Longitudinal bunch profile measurement of operational H^- beam using laser wire and virtual slit

Y. Liu,* C. Long, A. Shishlo, A. Aleksandrov, and D. Brown
Oak Ridge National Laboratory, Oak Ridge, Tennessee 37831, USA

R. Thurman-Keup and V. Scarpine
Fermi National Accelerator Laboratory, Batavia, Illinois 60510, USA

(Received 30 December 2022; accepted 20 March 2023; published 6 April 2023)

We propose and demonstrate a nonintrusive diagnostic technique for measuring longitudinal bunch profiles of an operational high-power hydrogen ion (H^-) beam in the Spallation Neutron Source (SNS) linear accelerator at Oak Ridge National Laboratory (ORNL). The technique consists of a laser wire formed by a picosecond pulsed laser beam and a virtual slit created by controlling the magnetic field of the electron detector. The virtual slit eliminates the influence of the transverse beam profile and size on the longitudinal bunch profile measurement. The effectiveness of the diagnostics is investigated first in numerical simulations followed by experimental demonstrations performed on the neutron production (1.4 MW on target) H^- beam at the SNS superconducting linac. The results from the present measurement method are verified by an independent measurement approach.

DOI: 10.1103/PhysRevAccelBeams.26.042801

I. INTRODUCTION

Accurate information on the longitudinal bunch profile is important for the verification of beam dynamics and optimization of accelerator performance [1]. Conventional beam shape monitors (BSMs) use a metal wire to transform the ion bunch temporal structure into the temporal structure of low-energy secondary electrons which is further analyzed using transverse deflection in an rf deflector [2–5]. The conventional BSM scheme cannot be applied to an operational ion beam since the length of the ion beam to be measured needs to be sufficiently short to avoid any damage to the metal wire. For accelerators using superconducting cavities, wire-based diagnostics are generally avoided since a broken metal wire can cause catastrophic damage to the cavity. Another concern is that the wire material spattered by the beam could deposit on the surface of the cavity.

Nevertheless, the information about the longitudinal distribution of the H^- bunch is particularly useful for the reduction of the beam loss induced by intrabeam stripping (IBS) [6,7] which is an important beam loss mechanism in the H^- linac in addition to classical beam losses caused by "off-energy" and "off-aperture" particles. The IBS occurs when one of the electrons in a hydrogen ion is stripped in a collision and the resultant neutral hydrogen atom is lost from the beam. This IBS-induced beam loss could be reduced by making the H^- bunch bigger in all directions and consequently lowering the probability of collisions. At the SNS linac, the transverse sizes of the H^- beam are optimized by controlling the field of the linac quadrupoles while the optimization of the bunch length remains as an unsolved task. An ability to measure longitudinal parameters of the H^- bunch along the superconducting linac (SCL) is very valuable for this optimization.

A schematic of the SNS linac [8] including SCL is shown in Fig. 1. The SCL consists of 23 cryomodules and 9 empty slots reserved for the linac power upgrade. The first 11 cryomodules contain 3 medium-beta rf cavities each and the remaining 12 cryomodules contain 4 high-beta rf cavities each. All 81 rf cavities have independent control of their phase and accelerating gradient. Cryomodules are separated by warm sections which contain quadrupole magnets and diagnostics. The beam energy profile along the linac is not fixed and can change from one operation run to another, or even within one run if the gradient of one or several cavities needs to be adjusted. The transverse and longitudinal beam parameters change with every retuning; therefore, a quick measurement of those parameters would facilitate the setup and operation of the SCL.

Currently, longitudinal bunch profiles of the H^- beam in the SNS SCL are measured using noninterceptive methods based on the physics model and the information from beam loss, beam current, or beam position monitors [11,12].

*liuy2@ornl.gov

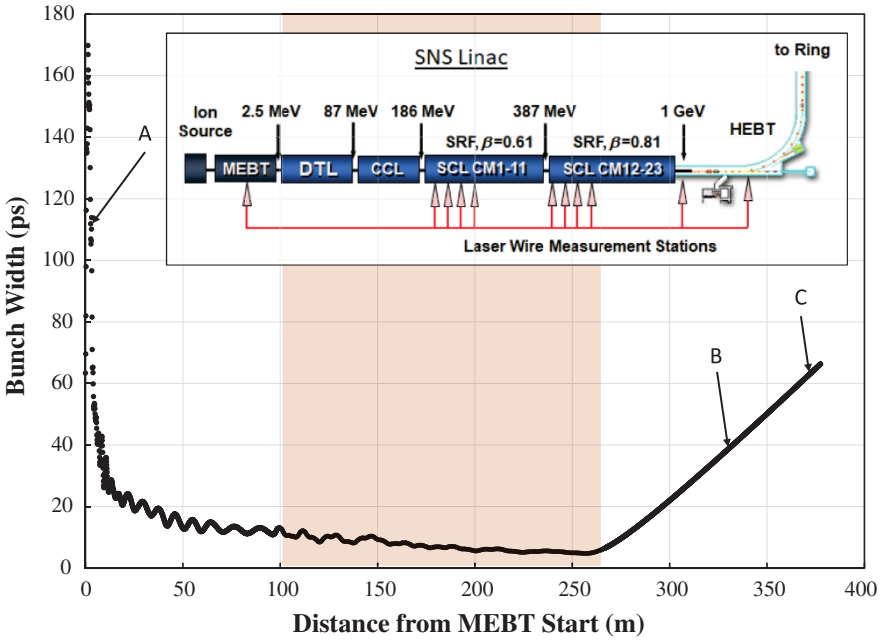

FIG. 1. Design values of H^- beam longitudinal bunch width at the SNS linac. Inset box: schematic of SNS linac. DTL: drift tube linac, CCL: coupled cavity linac, SRF: superconducting rf cavity, CM: cryomodule. The shaded region corresponds to the SCL section of the SNS linac. Laser wire–based longitudinal profile measurements were previously conducted at SNS MEBT [9] (location (A) and HEBT [10] (locations B and (C) where H^- beam bunch widths are typically an order of magnitude larger than the light propagation time through the ion beam. The virtual slit technique is proposed for the longitudinal profile measurement in the SCL section.

These methods can be used for H^- and proton linacs, but they have a few limitations. First, they require phase scan of the cavity and therefore are not applicable to the operational beam. Second, they have only been applied to the beginning of the SCL because they need a long downstream part to characterize the beam disturbed by the phase scan. As a result, longitudinal profiles in the later part of the SCL can only be obtained from models and cannot be verified. In addition, a more practical and easier approach described in [12] gives information only about the rms parameters of the bunch.

The concept of a bunch profile monitor using a laser wire technique was proposed decades ago [13] and the instrumentation was studied more recently at the medium energy beam transport (MEBT) [9] and high energy beam transport (HEBT) of the SNS linac [10] as well as at PIP2IT of Fermilab [14]. The measurement is based on the photoneutralization of the ion beam where the loosely bound electrons are detached from the hydrogen ions by a focused laser beam, often referred to as laser wire, and the number or density of the detached electrons leads to the determination of the original ion density. The laser-based bunch shape monitor (LBSM) is nonintrusive and can be performed on operational H^- beams. However, a major technical challenge has been identified in the development of the LBSM at the SCL of the SNS. As shown in Fig. 1, the design value of the longitudinal bunch width converges rapidly from ~100 ps at the MEBT to less than 10 ps at the SCL. This short bunch width in the SCL means the propagation time of the laser beam through the ion beam is not negligible compared to the bunch width and will introduce a contribution to the measured width. A mitigation solution is to deconvolve the effect of the beam transverse profile from the measured profile, but this approach strongly depends on the accuracy of the beam transverse profile measurement. Decoupling the influence of the transverse profile and size from the longitudinal profile measurement is therefore highly desirable to obtain reliable longitudinal profile measurements of short bunches.

In this paper, we propose and demonstrate a reliable LBSM technique for longitudinal profile measurement of high-energy, short-bunched H^- beam. By controlling the magnetic field in the electron detection, we can create a virtual slit to effectively decouple the effect of the transverse profile and size of the ion beam on its longitudinal bunch profile measurement. The virtual slit technique has a very simple implementation and requires no additional hardware. The method is applied to the longitudinal profile measurements of a neutron production H^- beam line at the SNS superconducting linac. The measurement performance is discussed through a comparison with an independent measurement approach.

The paper is outlined as follows: In the next section, we will review the principle of LBSM and illustrate the influence of the transverse dimension on the longitudinal profile measurement. In Sec. III, we describe how a virtual slit can be created by utilizing the detection scheme through

numerical simulations. In Sec. IV, we present the experimental results of the proposed method and discussions on the measurement performance. A summary is given in Sec. V.

II. MEASUREMENT PRINCIPLE

Laser-based H^- beam diagnostics is based on a light-ion interaction process referred to as the photodetachment. Irradiation of H^- beam with a laser light with photon energies above 0.75 eV causes the detachment of electrons from negative ions and the measurement of the resulting electron density leads to the determination of the negative ion density. The proposed LBSM method is schematically shown in Fig. 2. A high-energy H^- beam is intercepted by a laser beam at a normal incidence angle. The laser beam is weakly focused so that a narrow laser beam (laser wire) is interacting with the ion beam around its focal point. As a result of the photodetachment, a small portion (typically a few percent at the peak location) of the ions are neutralized. The inset box shows an example of the distribution of the photodetached electrons. The electrons are separated from the H^- beam by a dipole magnet installed right next to the laser-ion interaction region and guided into a Faraday cup (FC) used as an electron detector. For the LBSM discussed in this work, the laser pulses have the same repetition rate as the ion bunch, and the phase delay between laser and ion pulses is tuned with an rf phase shifter. The FC output obtained at different phases is used to reconstruct the longitudinal profile of the measured ion beam.

The outcome of the photodetachment, denoted as the density of photodetached electrons n_{pd}, is directly proportional to the product between photon and particle beam densities as

$$\frac{dn_{pd}(x,y,z,t)}{dt} = -\frac{dn_b(x,y,z,t)}{dt} = c\sigma n_b(x,y,z,t) n_l(x,y,z,t), \quad (1)$$

where c is the light speed, σ is the photon-ion interaction cross section, and n_b and n_l represent density functions of ion and photon beams, respectively. The photodetachment process has a weak dependence on the laser wavelength. For laser-based H^- beam diagnostics, lasers with a center wavelength of around 1064 nm (corresponding photon energy 1.16 eV) are most frequently chosen as the light source due to their market availability and easy integration with the fiber or solid-state optical amplifiers. For particle beam energies in the range of 0.4–1.0 GeV and a laser wavelength of 1064 nm (laboratory frame), σ varies between $3\text{–}4 \times 10^{-17}$ cm^2. Without loss of generality, we assumed $\sigma = 3.5 \times 10^{-17}$ cm^2 in the calculations. Since the bunch width is much smaller than the bunch period, the overall photodetached electrons from one ion beam bunch can be calculated by integrating n_{pd} over one period of the ion bunch

$$N_{pd}(s) = c\sigma \int_0^T \left[\iiint_{-\infty}^{\infty} n_b(x,y,z,t) n_l(x,y,z,t-s) dx dy dz \right] dt, \quad (2)$$

where s is the phase delay between the laser and ion pulses and T is the period of the ion bunch. For a demonstration of the basic principle, we ignore the depletion of the ion beam density due to photodetachment and further assume that both ion and laser beams have a Gaussian distribution in all directions, i.e.,

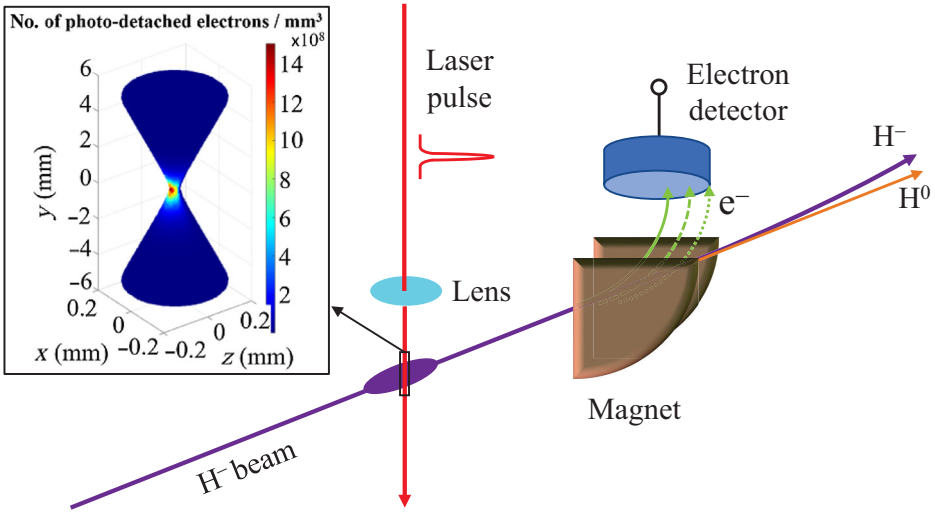

FIG. 2. Schematic of laser wire–based H^- beam longitudinal bunch profile measurement. H^- beam propagates in the z direction and the laser beam propagates in the y direction. The inset box shows an example of the distribution of the photodetached electrons in the laser-ion beam interaction region.

$$n_b(x,y,z,t) = \frac{N_b}{(2\pi)^{3/2}\sigma_{bx}\sigma_{by}\sigma_{bz}} \exp\left[-\frac{x^2}{2\sigma_{bx}^2} - \frac{y^2}{2\sigma_{by}^2} - \frac{(z-\beta ct)^2}{2\sigma_{bz}^2}\right], \tag{3}$$

$$n_l(x,y,z,t) = \frac{N_l}{(2\pi)^{3/2}\sigma_{lx}\sigma_{ly}\sigma_{lz}} \exp\left[-\frac{x^2}{2\sigma_{lx}^2} - \frac{(y-c(t-s))^2}{2\sigma_{ly}^2} - \frac{z^2}{2\sigma_{lz}^2}\right], \tag{4}$$

Here, N_b is the number of ions in one bunch, $\sigma_{bx,y,z}$ represent the rms size of the ion beam in space. N_l and $\sigma_{lx,y,z}$ are the corresponding parameters of the laser beam. Furthermore,

$$\sigma_{bz} = \beta c\tau_b, \tag{5}$$

$$\sigma_{ly} = c\tau_l, \tag{6}$$

where τ_b is the rms bunch width of the ion beam and τ_l is the rms pulse width of the laser beam. In this simplified case, the output of the photodetached electrons can be explicitly written as a function of the phase delay

$$N_{pd}(s) \propto \exp\left[-\frac{s^2}{2\tau_{\text{meas}}^2}\right] \tag{7}$$

with

$$\tau_{\text{meas}} = \sqrt{\tau_b^2 + \tau_l^2 + (\sigma_{lz}/\beta c)^2 + (\sigma_{by}/c)^2}. \tag{8}$$

Equation (8) reveals that the longitudinal bunch profile obtained from the photodetachment signal is essentially a convolution of the actual beam bunch with the laser pulse, the propagation of the laser beam through the ion beam, and that of the ion beam through the laser beam. An accurate longitudinal profile measurement requires (i) $\sigma_{lz} \ll \beta c\tau_b$, i.e., thin laser wire; (ii) $\tau_l \ll \tau_b$, i.e., narrow laser pulse width; and (iii) $\sigma_{by} \ll c\tau_b$, i.e., thin ion beam. Among the three constraints, the size of the laser wire is in the submillimeter range so its effect is negligible. The laser pulse width can either be chosen significantly small or be precisely characterized in advance. The constraint of the thin ion beam, however, is more difficult to meet since both the transverse profile and size of the ion beam are subject to the particle beam condition and the tuning of the accelerator. Creating a small beam size may lead to a mismatch in the rest of the linac, an increase of beam losses, and therefore will not be operationally accepted for the neutron-producing beam. Especially when an ion bunch has comparable dimensions in transverse and longitudinal directions, i.e., $\sigma_{by} \sim c\tau_b$, the measurement accuracy of the transverse profiles will significantly impact that of the longitudinal profile measurement. Moreover, the transverse profile of the ion beam has to be obtained through a separate measurement and there is no guarantee that the ion beam always has a well-defined Gaussian distribution so its effect may not be accurately accounted for by its rms size as in Eq. (8). Therefore, to achieve a high-accuracy longitudinal profile measurement, it is highly desirable to decouple the effect of the transverse profile and size from the measurement.

III. VIRTUAL SLIT TECHNIQUE

A. Detection of photodetached electrons

Here we describe a decoupling method that exploits the electron detection scheme. As shown in Fig. 2, the photodetached electrons in the laser wire measurement are bent in the vertical direction by a dipole magnet. The ORNL-customized C-shape dipoles have a maximum center magnetic field of nearly 20 mT. The actual magnetic field is adjusted to optimize the electron detection efficiency according to the beam energy at each laser wire measurement station. Details of the dipole magnet used in the laser wire measurement are given in previous work [15].

We have simulated the electron trajectories in a magnetic field. In the simulation, we assumed the laser pulse has a hyperbolic secant profile. Table I shows the parameters of the ion and laser beams used in the simulation. Those

TABLE I. Parameters of ion and laser beams used in the simulation of trajectories of the photodetached electrons in the magnetic field.

Parameter	Value
H^- beam	
Energy	471 MeV
Relative energy spread	10^{-3}
Bunch frequency	402.5 MHz
Bunch width (rms)	8.6 ps
Beam charge	80 pC
Horizontal beam size σ_{bx}	3.3 mm
Vertical beam size σ_{by}	2.7 mm
Beam direction	[0,0,1]
Laser beam	
Wavelength	1064.5 nm
Pulse width (rms)	2.8 ps
Pulse repetition rate	402.5 MHz
Pulse energy	0.1 mJ
Beam waist on lens	7 mm
Focal length of lens	200 mm
Beam direction	$[0,-1,0]$

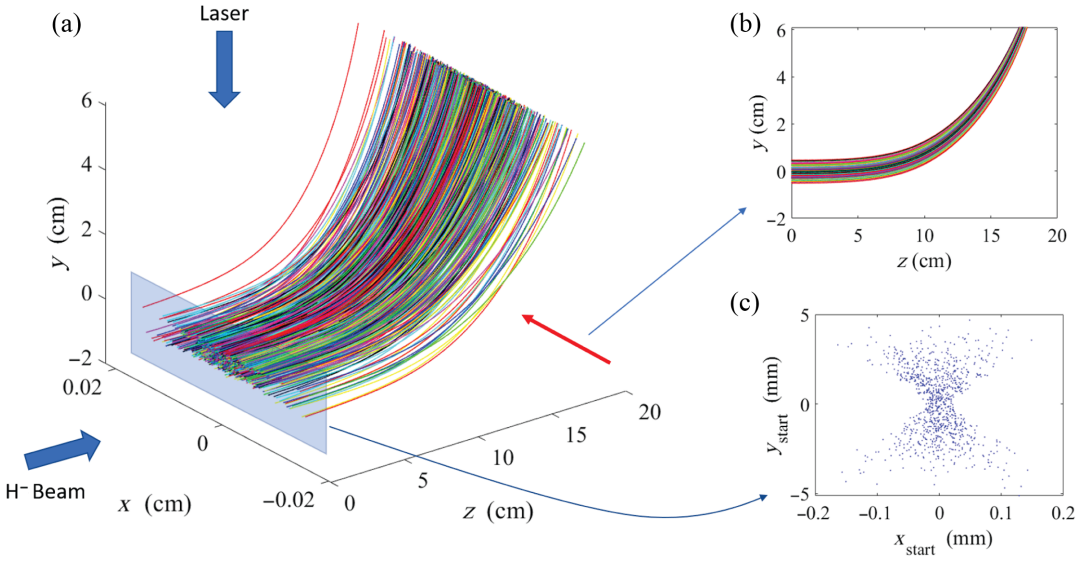

FIG. 3. (a) Three-dimensional trajectories of photodetached electrons in the magnetic field. (b) Trajectories as seen looking from the side. (c) Starting points of the trajectories in the x-y plane where one can see the laser beam waist.

values represent typical operational parameters at cryomodule 12 of the SNS superconducting linac.

The simulation is written in matlab and consists of two parts: the calculation of the number and positions of the photodetached electrons and the tracking of the electrons through the magnetic field to the FC. The calculation of the photodetached electrons uses a 3D rectangular grid through which the ion beam and laser propagate. The time steps are chosen to match the motion of the ions from one grid point to the next to facilitate the depletion of the ion beam which has a much lower density than the laser. At each step, the number of photodetached electrons at each grid point is calculated using the ion and laser densities at that grid point and photon-ion interaction cross section (see Fig. 2). Once the electrons have been generated, they are tracked through the fields of both the ion beam and the C-magnet. The field of the ion beam is calculated at the start and then spatially propagated in time during the simulation. The field of the C-magnet is evaluated using the commercial software cst and remains fixed during the simulation. Since the number of photodetached electrons is only ~1% of the H^- ion beam, the field of the photodetached electrons is expected to be small and is not included in the simulation. An independent simulation was done to verify this assumption. The tracking uses an adaptive fourth-order Runge-Kutta method which adapts the step size to limit changes in the direction and momentum of the electrons. Figure 3 shows the trajectories of the photodetached electrons in the magnetic field. In plot 3(c), one can also see the laser beam waist in the initial positions of the electrons.

To separate the transverse profile from the longitudinal profile, we make a mapping between the initial positions of the electrons in the laser-ion interaction plane and the final positions in the entrance plane of the FC as shown in Fig. 4. One obtains a linear relationship between the final and initial positions of the electrons although the beam width in the x direction and energy spread causes a very small spread in the position. As the magnetic field decreases, the electrons will move downstream on the entrance plane of the FC as shown in the figure. At a certain point, some of the electrons miss the detector. Figure 5 shows the detected electrons as a function of the magnetic field for a FC with a 5-cm aperture.

B. Effect of magnetic field on longitudinal bunch profile measurement

The above simulation shows that the amount of photodetached electrons detected by the FC can be controlled by

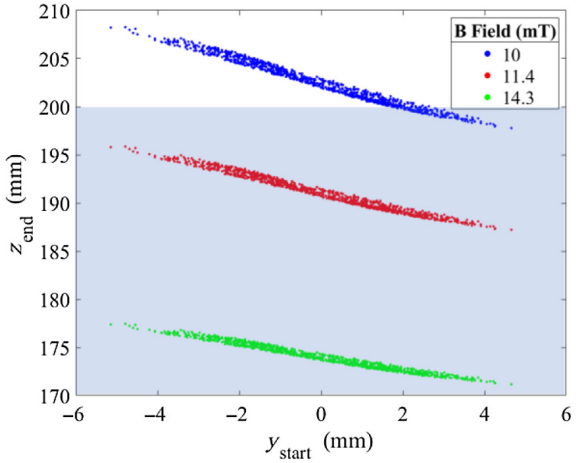

FIG. 4. Mapping between the initial position (y_{start}) and final position (z_{end}) of the electrons. The shaded region shows the FC aperture. The FC has a ϕ5-cm aperture with a center position at 175 mm. At a magnetic field value of 10 mT (corresponding to a coil current of 7 A), most of the electrons are not intercepted by the FC.

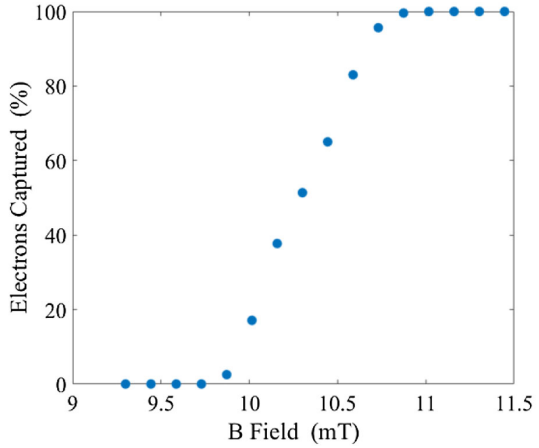

FIG. 5. Electron collection efficiency versus B field of the electron collection magnet. The B field is linearly proportional to the magnet current with a coefficient 1.43 mT/A.

the field strength of the dipole magnet. For the typical parameter set of an operational ion beam, there is a linear mapping between the initial positions of the photodetached electron in the laser-ion interaction plane and the final positions in the plane of the FC aperture. In particular, by properly scanning the magnetic field over a proper range such as the one shown in Fig. 4, one can use the FC aperture to select the photodetached electrons along the laser propagation direction, i.e., the y axis in Fig. 2. The concept can be expressed by a modified form of Eq. (2) as

$$N_{pd}(s;B) = \int_{-\infty}^{u(B)} P(s;y)dy, \tag{9}$$

where

$$P(s;y) = c\sigma \int_0^T \left[\iint_{-\infty}^{\infty} n_b(x,y,z,t) n_l(x,y,z,t-s) dxdz \right] dt. \tag{10}$$

Here, u is the cutoff position on the FC aperture of the electron beam. From Fig. 4, we know that u is a monotonic function of the magnetic field B. For practical implementation, it is more convenient to use the electron detection efficiency $\varepsilon(B)$ to account for the effect of the magnetic field. $\varepsilon(B)$ is defined as

$$\varepsilon(B) = \frac{\int_0^T N_{pd}(s;B)ds}{\int_0^T N_{pd}(s)ds}. \tag{11}$$

We first use numerical simulations to study how the measured bunch width varies at different electron detection efficiencies. During the simulation, we calculate $N_{pd}(s)$ at each cut-off position based on Eqs. (9) and (10). The obtained values of $N_{pd}(s)$ are then used to (i) estimate the bunch width τ_{meas} through fitting with a Gaussian function based on Eq. (7) and (ii) calculate the detection efficiency ε based on Eq. (11). Figure 6 shows the measured bunch width and cutoff position as a function of the detection efficiency. Two types of transverse profiles of the ion beam were used in the simulation. Type A profile is a standard Gaussian distribution while type B profile represents a non-Gaussian distribution with a long tail as often seen in a high-intensity linac. For type A beam profile, τ_{meas} is monotonically converging toward the real bunch width as ε decreases. This is expected since the influence of the ion beam transverse size decreases in proportion to ε. For type B beam profile, the dependence on the detection efficiency is not monotonic due to the complicated distribution,

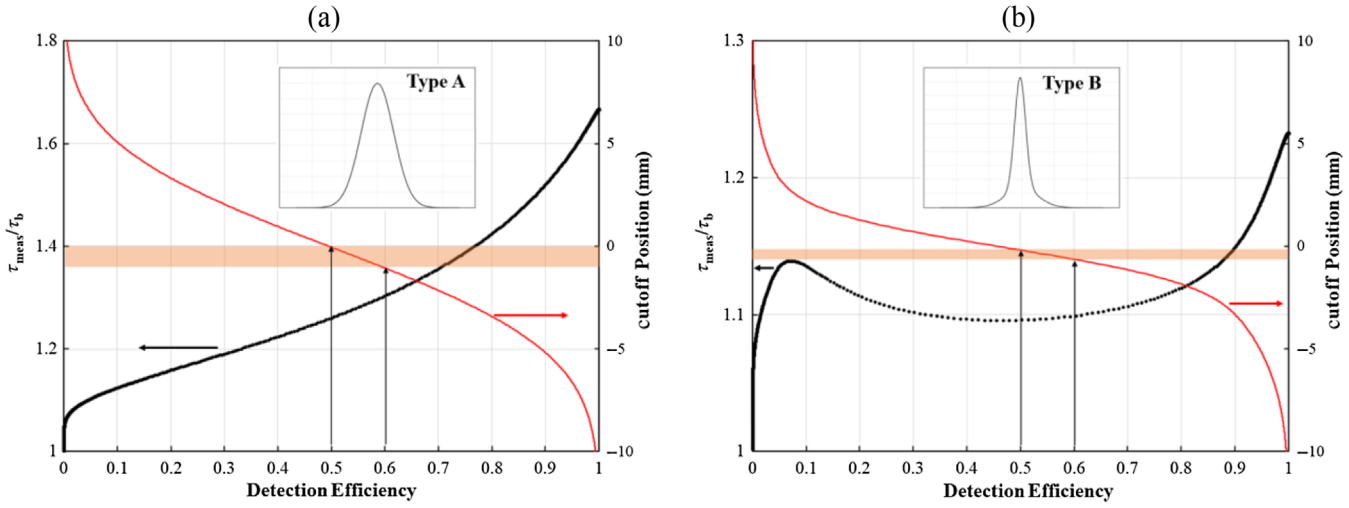

FIG. 6. Measured beam bunch width (black dots) and cutoff position (red lines) versus detection efficiency for (a) type A (Gaussian) and (b) type B (non-Gaussian) profiles of the H^- beam. The shaded region indicates a virtual slit that can be created by taking the difference between profiles measured at detection efficiencies of 60% and 50%. Inset boxes: transverse beam profiles with an rms size of 3 mm in both cases.

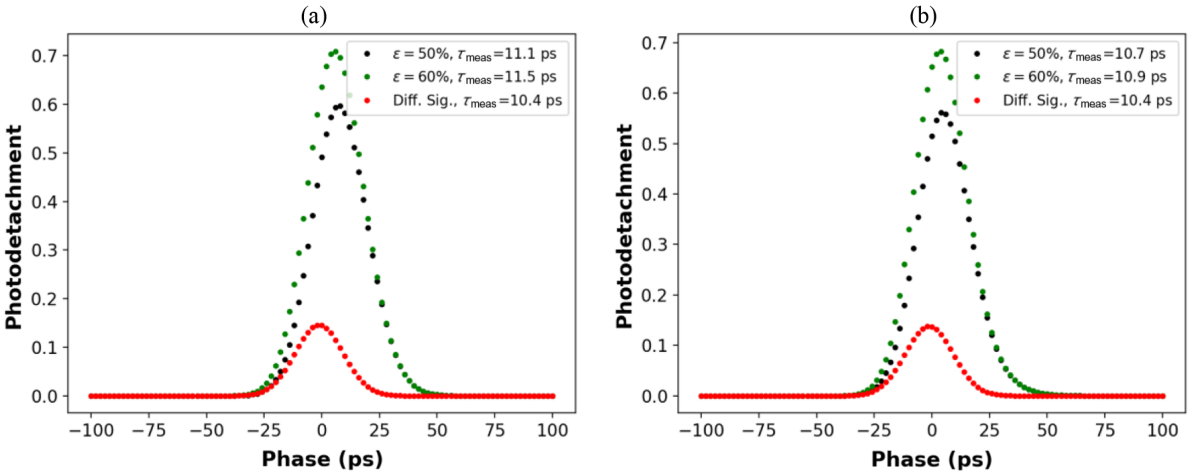

FIG. 7. Measured longitudinal profiles at 50% and 60% detection efficiencies and the differential profile. (a) Standard Gaussian profile and (b) non-Gaussian profile. The photodetachment output in the figure is normalized to the value obtained at $\varepsilon = 100\%$.

as shown in Fig. 6(b). In both cases, however, the measured bunch width approaches the actual bunch width value as $\varepsilon \to 0$, i.e., $u \to -\infty$ which indicates that the laser beam intersects a particle beam with an infinitesimal size.

C. Creation of virtual slit

It is quite clear that by controlling the dipole magnet, one can reduce the number of the photodetached electrons in the detector and consequently reduce the effective transverse beam size of the ion beam. While in principle one can achieve a sufficiently small transverse size of the ion beam by directly reducing the magnet current, this approach will result in a very small detection signal and consequently cause a problem of low signal-to-noise ratio in the actual measurement. A more practical approach is to measure the profiles at different magnetic fields in the transition slope as shown in Fig. 5 and take the difference between the two profiles. The idea is very straightforward when the difference is small, as one can easily find out from Eq. (10) that the derivative of the position-dependent FC output with respect to B,

$$\left.\frac{\Delta N_{pd}(s;B)}{\Delta B}\right|_{\Delta B\to 0} = P(s;y)|_{y\equiv u(B)}, \tag{12}$$

corresponds to a signal that does not contain the propagation time of the laser beam through the ion beam. In the actual application, the derivative value can be approximated by taking the difference between profiles measured at two different magnetic fields.

In Fig. 7, we show two simulation results of the longitudinal profiles measured on the ion beams with type A and B transverse profiles as shown in Fig. 6. In each case, we show the measured profiles measured with $\varepsilon = 60\%$ and $\varepsilon = 50\%$ and the differential profile between the two. The measured bunch width from both examples shows a perfect agreement with the actual bunch width after deconvolving the effect of the laser pulse width ($\tau_l = 2.8\ ps$ used in the simulations).

The proposed method corresponds to an installation of a narrow slit on the aperture of the FC. In other words, a virtual slit is created by taking the difference of the FC outputs between two detection efficiencies, or two magnet currents, as schematically shown in Fig. 6. The width of the virtual slit can be calculated using

$$w_{vs} = u(B_2) - u(B_1). \tag{13}$$

Figure 8 shows the width of the virtual slit as a function of the detection efficiency difference $\Delta\varepsilon = \varepsilon(B_2) - \varepsilon(B_1)$. The corresponding bunch width measurement error, defined as $\frac{\tilde{\tau}_b - \tau_b}{\tau_b} \times 100$ (τ_b: actual, $\tilde{\tau}_b$: measured), is also

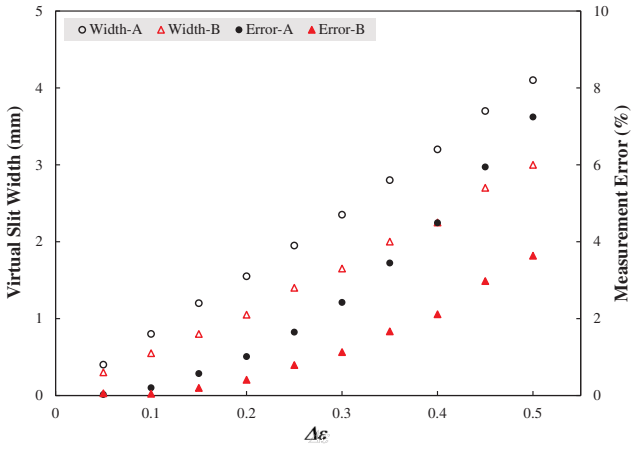

FIG. 8. Equivalent size of virtual slit and the corresponding measurement error versus $\Delta\varepsilon$ used in the creation of virtual slit. A and B correspond to two different transverse profiles of the ion beam (see Fig. 6) used in the simulation.

plotted to show the effect of the virtual slit. A 1.5-mm virtual slit is formed by taking the difference as large as $\Delta\varepsilon = 20\%$ and this virtual slit will result in a very small measurement error (within 1%). It is noted that the virtual slit is not subject to the influence of particle beam energy or power and has no dependence on the transverse beam shape or size.

IV. EXPERIMENTAL RESULTS

The virtual slit technique has been applied to the profile measurement of 1-GeV, 1.4-MW operational H^- beam at the SCL of SNS. Currently, a total of nine laser wire stations are installed in the warm sections of the first four medium-beta cryomodules, i.e., LW1-4, the warm sections of the first high-beta cryomodules, i.e., LW12-15, and the warm section of the last cryomodule slot, LW32.

A. Laser wire system

A customized laser was recently developed as the light source for the laser wire-based H^- beam diagnostics at the SNS linac [16]. The laser was built based on a master oscillator power amplifier (MOPA) design with a mode-locked seed laser and solid-state amplifiers. For the longitudinal bunch profile measurements in this work, we used a mode-locked fiber laser (Calmar PSL-01UFF) which has a FWHM pulse width of 6–10 ps and a center wavelength of 1064.5 nm. Laser pulses were synchronized to the external 402.5 MHz rf signal and the phase delay could be continuously adjusted by a phase shifter over an entire period. The seed output was first amplified by a fiber amplifier to obtain a pulse energy of about 0.25 nJ. The output was then coupled into a free-space acousto-optic modulator (AOM) to form macropulses. The selected macropulses were amplified by three stages of diode-pumped, double-passed Nd:YAG amplifiers. The pump current and pulse duration of each amplifier were carefully tuned to achieve necessary laser power with near diffraction-limited beam quality to allow proper propagation of the laser beam through a long free-space transport line. The customized laser system outputs 60-Hz macropulses and each macropulse contains 10–40 micropulses at 402.5 MHz with a peak power adjustable up to more than 100 MW. An example of the laser pulse waveform is shown in Fig. 9.

The laser system is located outside the accelerator tunnel and the laser beam is delivered to the measurement locations through a free-space transport line. An active feedback system is used to stabilize the laser beam position [15]. The laser beam spot size with diameters of 5–10 mm is typically formed in front of the measurement chamber. Figure 10 shows the setup of a laser wire measurement station. For longitudinal profile measurement, the laser beam is incident from above the beam pipe to enable an effective trajectory control of the photodetached electrons in the dipole magnet. A lens (not shown) is installed in front of the laser port to focus the laser beam at the center of the beam pipe. Ion beam position is monitored at the end of each laser wire measurement chamber by stripline BPMs. The BPM data will be used to estimate the longitudinal bunch width and the result will be used to cross-check the LBSM measurement as discussed later.

The macropulsed laser system makes it possible to generate photodetached electrons from only a few laser pulses, which greatly improved the dynamic range of the signal. Due to the limited bandwidth of the detector, all electrons generated during one macropulse of the laser

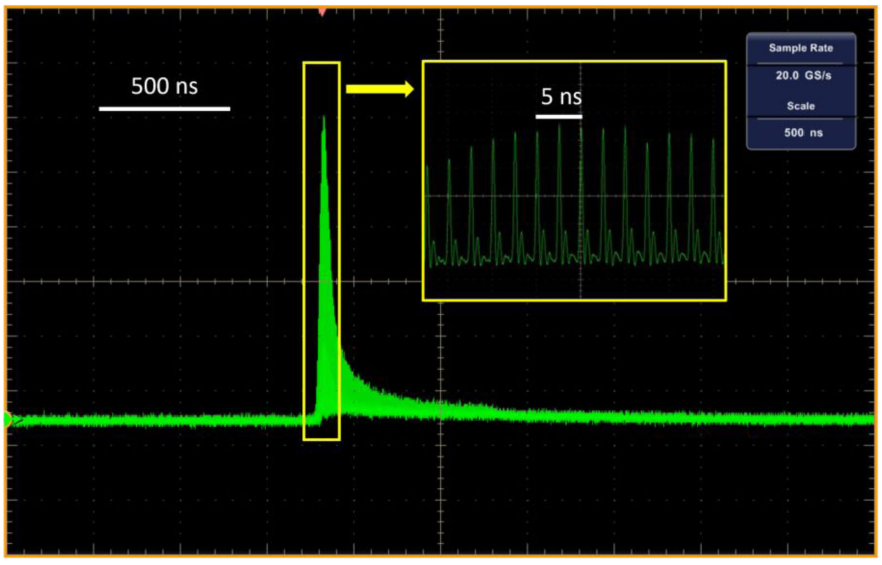

FIG. 9. An example of the laser pulse waveform. There are about 40 micropulses in one macropulse. Pulse energy is tunable up to 1 mJ. The macropulse repeats at 60 Hz. Small peaks in the pulse waveform in the inset box are due to the limited bandwidth of the photodetector.

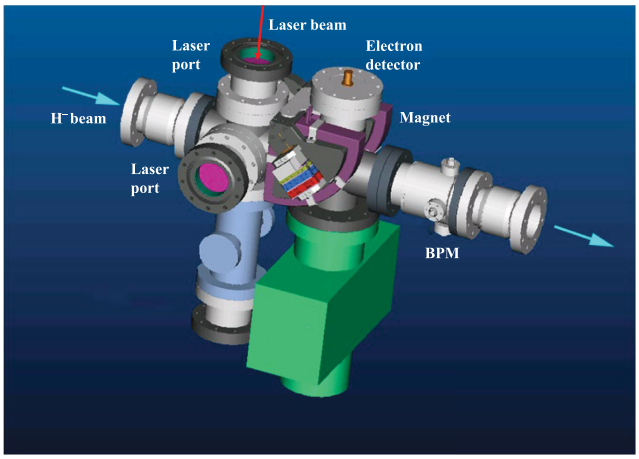

FIG. 10. Laser wire measurement setup in the SNS superconducting linac.

beam are detected as one signal. The FC output is digitized using a National Instruments (NI) PCI-5124 card at a sampling rate of 200 mega samples/ sec. Data acquisition was conducted at 60 Hz. At each phase delay value, ~10 samples were taken to obtain the average. The longitudinal bunch profile is reconstructed from the averaged FC output as a function of the phase delay with a resolution of 0.5 ps. A typical longitudinal profile scan for an operational H^- beam takes about 1 min to complete.

B. Profile measurements on neutron production H^- beam at SNS superconducting linac

Here we describe the profile measurement results on the neutron production (1.4 MW on target) H^- beam at measurement stations LW12 and LW15. The corresponding beam energies at the two locations are 471 and 590 MeV, respectively. The transverse profiles of the H^- beam were first measured using the laser wire and the results are shown in Fig. 11. Also plotted are the fitted curves based on the Gaussian function. Obviously, both profiles do not have a perfect Gaussian distribution, which is quite normal for high-power small size beams. The horizontal profile in particular has a significant tail. The rms beam sizes were calculated from the experimental data.

Prior to each longitudinal profile measurement, the dipole magnet for the electron detector was optimized to obtain a longitudinal profile with the maximum detection efficiency, and the corresponding magnet current I_0 was used as the reference. The magnet current was then adjusted so that a transition slope such as the one shown in Fig. 5 was observed. Figure 12 shows six longitudinal profiles measured at different magnet currents. Each dot in the figure represents an average from ten measurement samples. Clearly, all measured profiles were well fitted with Gaussian functions. The measured bunch width τ_{meas} as well as its standard deviation were calculated from the measurement data using a standard curve fitting procedure.

Figure 13 summarizes the detection efficiency (calculated from the integration of the profiles and normalized to its maximum value) and the measured bunch width as a function of the magnet current. We observed a sharp change in the detection efficiency over the magnet currents of 0.7–0.8 I_0, which agreed well with the simulation results in Fig. 5. The measured bunch width decreases as the magnet current changes from 10 to around 7.5 A but then increases when the magnet current is further reduced. This is also consistent with the theoretical prediction for a non-Gaussian transverse profile as shown in Fig. 6(b).

Figure 14 shows two examples of the application of the virtual slit technique. The first virtual slit was created by taking the differential signal between the profiles obtained at 7.6 and 7.4 A. The corresponding detection efficiencies are 53% and 39% for the two magnet currents, respectively. From the differential profile, we obtained $\tau_{\mathrm{meas}} = 10.8 \pm 0.62$ ps as shown in Fig. 14(a). The second virtual slit was

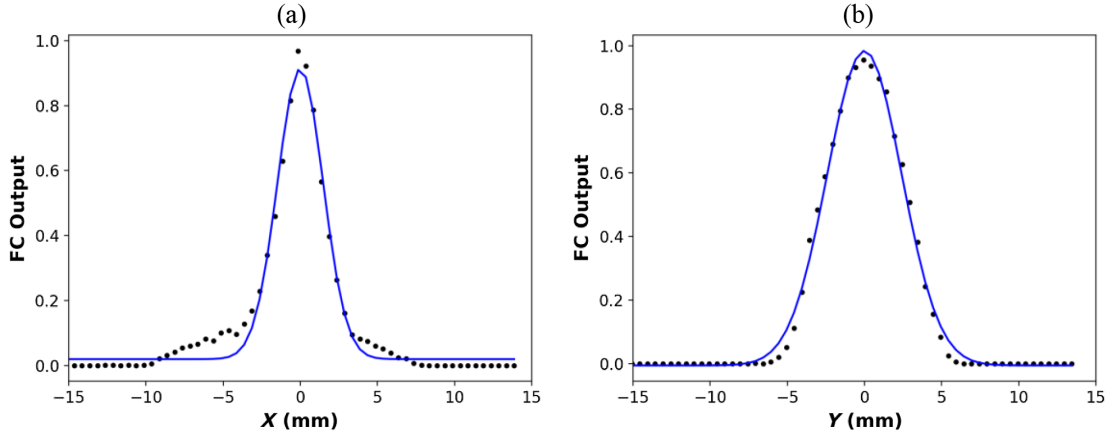

FIG. 11. (a) Horizontal and (b) vertical profiles measured at SCL LW12 using laser wire. Dots are the measured data and lines are the fitted Gaussian curves. RMS beam size is 2.17 mm for horizontal and 2.19 mm for vertical profiles. FC output is normalized to the peak value.

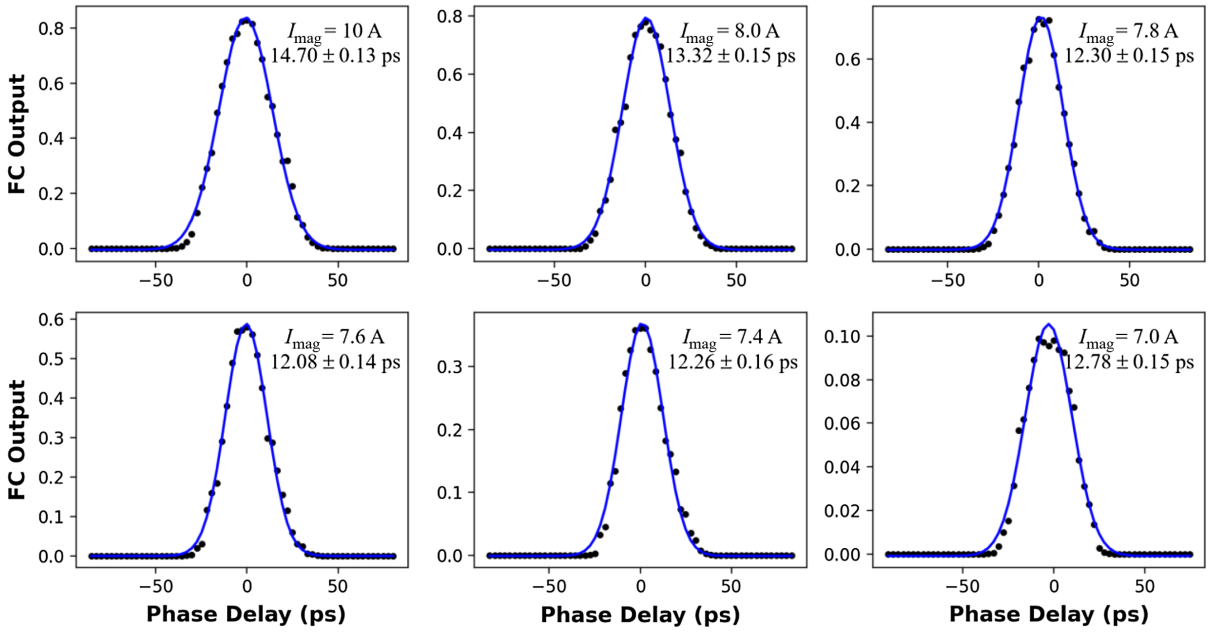

FIG. 12. Longitudinal profiles of the 1.4-MW operational H^- beam at SCL LW12 measured at different magnet currents. Dots are the measured data and lines are the fitted curves from Gaussian functions. Magnet current and measured bunch width τ_{meas} are shown in each subplot. Error bars of individual data points were not shown in the plots for clarity but were used in the estimation of τ_{meas} and its error. FC output in the figures is normalized to its value at the maximum collection efficiency.

formed by using the differential signal between the profiles obtained at 7.4 and 7.2 A (corresponding detection efficiency of 22%). We obtained $\tau_{meas} = 10.53 \pm 0.49$ ps from the new slit as shown in Fig. 14(b). It is noted that the two virtual slits result in a very close bunch width estimation which is consistent with the measurement results from other method, as will be discussed in the next section. The τ_{meas} obtained from the differential profiles has a larger error than those obtained from individual profiles. This is because the standard deviation of each data point in the differential profile was calculated as an add-in-quadrature of their counterparts in the two individual profiles. We also directly deconvolved the effect of the vertical beam size from the measured profile at the maximum detection efficiency. The calculated bunch width $\sqrt{\tau_{meas}^2 - (\sigma_{by}/c)^2} = 12.76$ ps from the direct deconvolution is quite different from the values obtained from the current virtual slit approach.

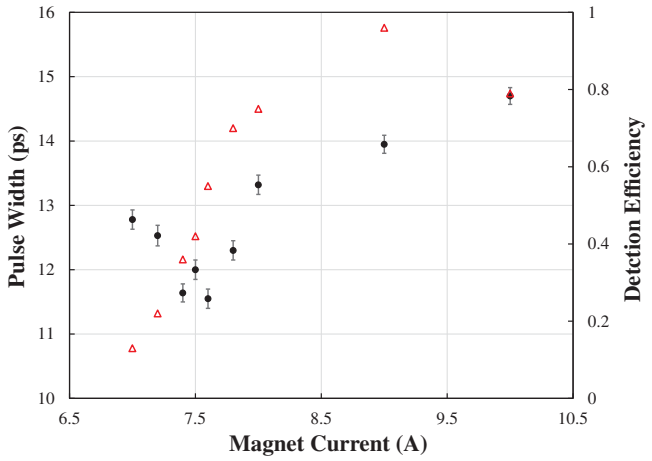

FIG. 13. Detection efficiency and measured bunch width as a function of the magnet current. Solid dots with standard deviation error bars are the bunch width obtained from the fitted curves and triangles are the detection efficiency. The detection efficiency drop beyond 9 A might be due to the misalignment among the beam, dipole magnet, and FC.

The longitudinal profile measurement results at the laser wire measurement station LW15 are summarized in Fig. 15. Figure 15(a) is the measured vertical transverse profile. Note that the vertical profile at LW15 has a longer tail than that in LW12. Figure 15(b) shows the longitudinal profile measured at the maximum detection efficiency obtained at the magnet current $I_0 = 11$ A. The detection efficiency as well as the value of τ_{meas} are plotted in Fig. 15(c) as a function of the magnet current. Once again, we observed a sharp change in the detection efficiency over the magnet current range 0.7–0.8 I_0. A virtual slit was created by taking the difference between profiles measured at 8.8 (corresponding detection efficiency 43%) and 8.6 A (corresponding detection efficiency 25%) and the results are shown in Fig. 15(d). The bunch width measured from the virtual slit is 9.03 ± 0.76 ps which is close to the design value.

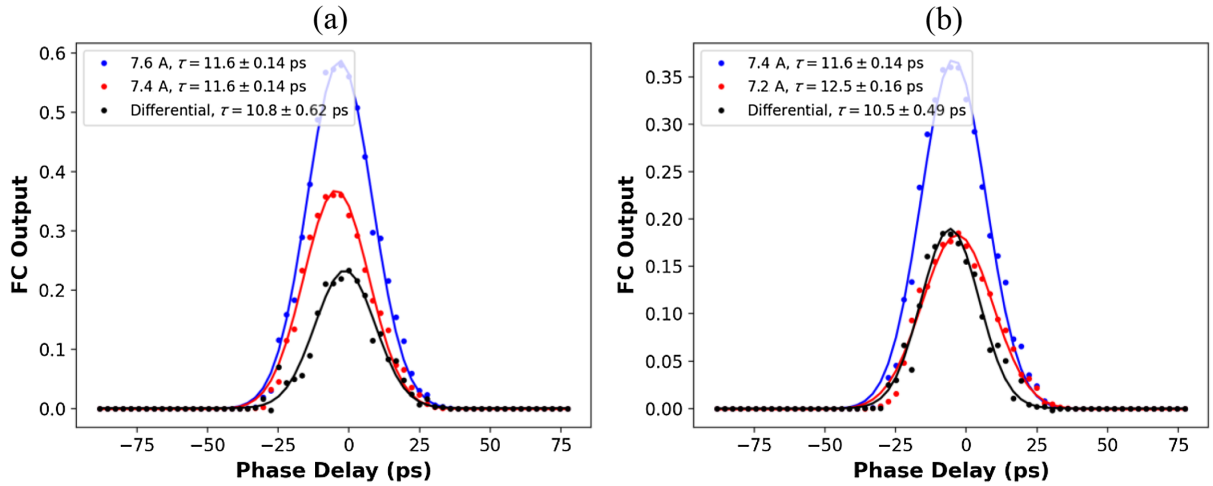

FIG. 14. (a) Longitudinal profiles measured at magnet currents 7.4 and 7.6 A and the differential profile and (b) longitudinal profiles measured at magnet currents 7.2 and 7.4 A and the differential profile. Dots are the measured data and lines are the fitted curves of Gaussian functions. FC output in the figures is normalized to the maximum collection efficiency.

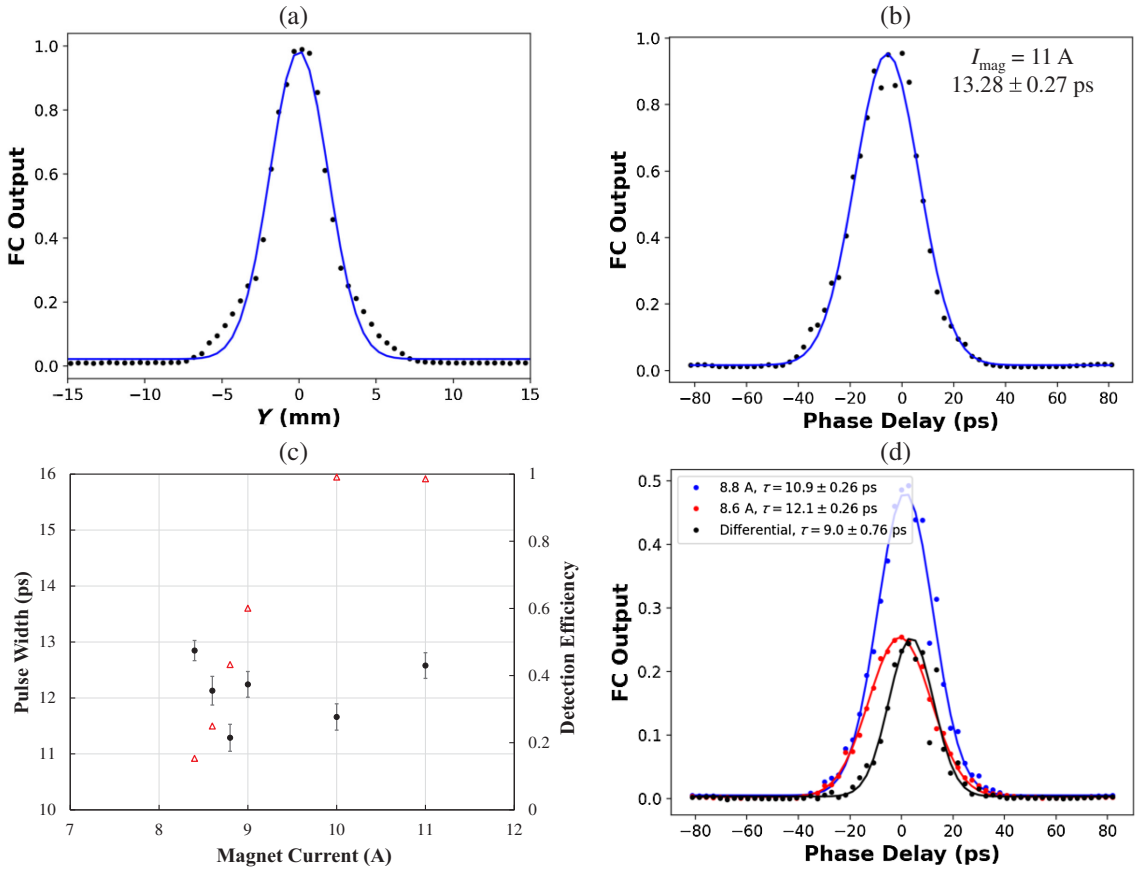

FIG. 15. Measurement results at LW15 of SNS linac. (a) Vertical profile with rms beam size of 2.56 mm, (b) longitudinal profile measured at the maximum detection efficiency, (c) detection efficiency and bunch width as a function of the magnet current, (d) longitudinal profiles measured at magnet currents 8.8, 8.6 A, and the differential profile. Dots are the measured data and lines are the fitted curves of Gaussian functions. FC output in the figures is normalized to its value at the maximum collection efficiency.

C. Comparison with bunch width measurement using stripline BPMs

To validate the measurement results and investigate the limitations of the proposed diagnostic technique, we have conducted a series of experiments to compare the bunch width measurement results from the current method with the results obtained from a BPM-based approach previously developed at SNS [12]. In the BPM-based approach, the signals from stripline BPMs are collected in a process of superconducting cavity phase scan. During this scan, all downstream cavities should not have the rf power in them. In addition to the transverse beam position, the BPMs' signals include the phase of bunches relative to the rf signal reference line and the amplitude of Fourier transformation for the longitudinal density of the bunch. The procedure and limitations are described in [17]. For the neutron production settings, the results of these measurements for SCL cavities 11c, 12a–12d, and 13a are shown in Fig. 16. We also plotted the bunch width of the 1.4-MW neutron production H^- beam using the present laser wire and virtual slit technique. The laser wire measurement result at LW12 shows an excellent agreement with the BPM measurement results at Cav12d and Cav13a.

Further comparisons between two methods have been made with more dedicated experiments. Since the BPM-based measurement approach requires all downstream cavities be turned off, the experiments were only conducted on a 1-μs, 5-Hz H^- beam pulse. In the first part of the experiment, all cavities prior to SCL cryomodule 12 were put at the neutron production setting while the synchronous phases of cavities 12a–12d were set at −6.40°, −6.50°, −5.00°, −8.50°, respectively. In the meantime, we adjusted the magnetic field gradient of quadrupole QV11 to create four different transverse beam sizes at LW12. The predicted bunch width from [12,17] was 9.14–10.01 ps for the above quadrupole settings. In the second part of the experiment, quadrupole QV11 was put back to the production setting while the synchronous phases of cavities 11c–12a were set to be −25° to squeeze the bunch. The model predicted a bunch width of ∼4.5 ps would be obtained at LW12 at this condition. Note that the bunch squeeze is also accompanied with a substantial change in the beam transverse profile and size at LW12.

At each of the above settings, we measured both the transverse and longitudinal profiles of the ion beam using the present laser wire technique. The results are summarized in Fig. 17. Since each setting resulted in a different transverse size of the beam, we plotted the measured bunch widths obtained both with and without using the virtual slit as well as the predicted bunch width values as a function of the measured vertical beam size. The first four datasets in Fig. 17 correspond to four different settings of QV11 used in the first part of the experiment while the right-most dataset in the figure is the measurement results of the squeezed beam bunch achieved in the second part of the experiment.

Since the experiment was conducted at low repetition rates, only 3–5 samples were taken at each phase delay so the standard deviations of individual data points are larger compared to the case of the 60-Hz operational beam. As a result, the measured bunch width shows larger error bars

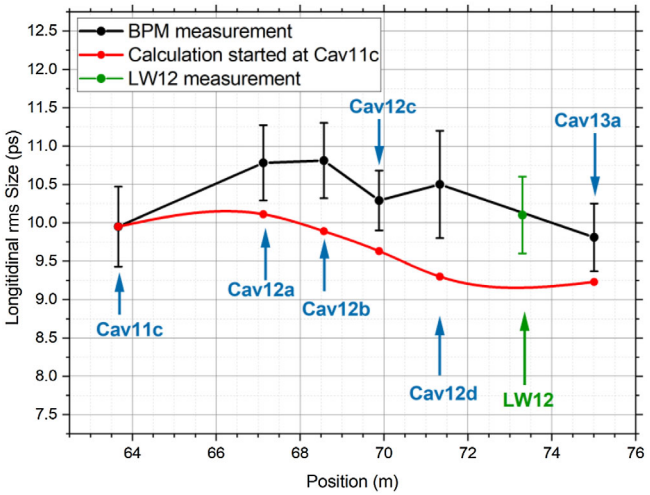

FIG. 16. Beam bunch width at different cavities for the initial (production) settings. The black points are the results of BPM data analysis for each cavity, and the red curve is a simulation result for tracking longitudinal Twiss parameters at cavity 11c downstream to cavity 13a. The green dot is the bunch width of the neutron production beam measured using the present laser wire and virtual slit technique. Position starts from the beginning of SCL.

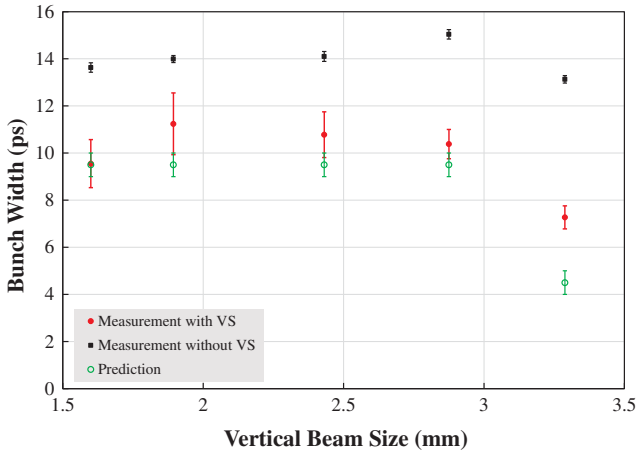

FIG. 17. Bunch width versus rms vertical beam size measured at different quadrupole and cavity settings. From left, the first four datasets correspond to the quadrupole QV11 settings of 3.85, 3.6, 3.37 (production setting), and 3.1 T/m, respectively. The right-most dataset corresponds to the condition when the synchronous phases of cavities 11c–12d were set to −25° while QV11 was at the production setting. Green circles are the bunch width values predicted from the BPM-based method [12,17]. VS: virtual slit.

than those measured from the operational beam. Nevertheless, the bunch width measured with virtual slit gave close values to the predicted range although the transverse beam size changed more than 70%. The results verified that the virtual slit technique can effectively remove the influence of the transverse beam size on the longitudinal profile measurement.

On the other hand, the measurement result of the squeezed beam bunch (the right-most dataset in Fig. 17) shows a large discrepancy (7.3 versus 4.5 ps) between the measurement and predicted values. We consider the large discrepancy could be due to several factors: (i) a relatively large laser pulse width (rms width ~3 ps) was used in the measurement; (ii) inaccurate prediction of the model (we used an rms envelope code, which can have significant errors near the tight focus of the beam with non-Gaussian distributions). (iii) laser pulse temporal instability generated during amplification. Mitigation measures including reduction of laser pulse width, improvement of modeling and laser pulse stability are currently being researched to improve the measurement performance.

V. SUMMARY

Laser wire has been proposed as a nonintrusive approach for beam diagnostics in high-intensity particle beam accelerators. While the principle was demonstrated decades ago, the actual implementation and the coupling between the transverse and longitudinal dimensions remained as challenges for accurate measurement in the longitudinal domain. The challenge is especially severe for the measurement of short bunches such as in the SNS superconducting linac where the travel time of the laser beam through the ion beam is comparable to the longitudinal bunch width itself. In this paper, we presented a novel approach that exploits the detection scheme in the laser wire measurement. A virtual slit can be created by properly taking the difference of the measured profiles between two magnet currents. The virtual slit can effectively eliminate the influence of the transverse beam profile and size on the longitudinal profile measurement. The method does not require additional hardware installation and has a large tolerance to the actual difference between detection efficiencies (or magnet currents) and therefore can be easily implemented. We have applied the method on the neutron production H^- beam (1.4 MW on target) at the SNS superconducting linac and the results showed a good agreement for the bunch width within the range of production setting.

Although this paper only described the measurement results at two locations of the linac, the proposed method has been applied to other laser wire measurement stations (Fig. 1) along the SCL and HEBT. The measurement results can provide an additional tool for cavity tuning and beam loss reduction in superconducting linac, which is particularly important as SNS is currently ramping up the beam power toward 2 MW with a total of 28 new superconducting cavities being added to the linac. Furthermore, by measuring longitudinal profiles using the laser wire at different phase conditions of the superconducting cavity, we have measured for the first time the longitudinal emittance of the beam at its production setting. Those measurement results will be published elsewhere.

ACKNOWLEDGMENTS

The authors acknowledge the support from Sarah Cousineau and technical help from Andy Webster and Syd Murray III. This research used resources at the Spallation Neutron Source, a U.S. Department of Energy (DOE) Office of Science User Facility operated by the Oak Ridge National Laboratory. This work was supported by the U.S. DOE under Contracts No. DE-AC05-00OR22725 and No. DE-AC02-07CH11359. The U.S. government retains and the publisher, by accepting the article for publication, acknowledges that the U.S. government retains a nonexclusive, paid-up, irrevocable, worldwide license to publish or reproduce the published form of this manuscript, or allow others to do so, for U.S. government purposes. DOE will provide public access to these results of federally sponsored research in accordance with the DOE Public Access Plan [18].

[1] P. Strehl, *Beam Instrumentation and Diagnostics* (Springer-Verlag, Berlin, Heidelberg, 2006), Chap. 7.

[2] A. V. Feschenko, L. V. Kravchuk, A. A. Menshov, A. V. Aleksandrov, S. Assadi, J. Galambos, and S. Henderson, Longitudinal beam parameters study in the SNS linac, in *Proceedings of the 22nd Particle Accelerator Conference, PAC-2007, Albuquerque, NM* (IEEE, New York, 2007), THOAAB01, pp. 2608–2610.

[3] A. Miura *et al.*, Bunch shape measurement of 181 MeV beam in J-PARC Linac, JPS Conf. Proc. **8**, 011003 (2014).

[4] S. A. Gavrilov and A. Feschenko, Design and development of bunch shape monitor for FRIB MSU, in *Proceedings of 6th International Beam Instrumentation Conference, IBIC2017, Grand Rapids, MI* (JACoW, Geneva, Switzerland, 2017), TUPCC13, pp. 179–181.

[5] V. Tzoganis, A. V. Aleksandrov, and R. Dickson, Present status and upgrades of the SNS ion beam bunch shape monitors, in *Proceedings of the 4th North American Particle Accelerator Conference NAPAC2019, Lansing, MI* (JACoW, Geneva, Switzerland, 2019), THZBB05, pp. 968–970.

[6] V. Lebedev, N. Solyak, J. F. Ostiguy, A. Aleksandrov, and A. Shishlo, Intrabeam stripping in H^- linacs, in *Proceedings of the 25th International Linear Accelerator Conference, LINAC-2010, Tsukuba, Japan* (KEK, Tsukuba, Japan, 2010), THP080, pp. 929–931.

[7] A. Shishlo, J. Galambos, A. Aleksandrov, V. Lebedev, and M. Plum, First Observation of Intrabeam Stripping of

Negative Hydrogen in a Superconducting Linear Accelerator, Phys. Rev. Lett. **108**, 114801 (2012).

[8] S. Henderson *et al.*, The Spallation Neutron Source accelerator system design, Nucl. Instrum. Methods Phys. Res., Sect. A **763**, 610 (2014).

[9] A. Zhukov, A. Aleksandrov, and Y. Liu, Longitudinal laser wire at SNS, in *Proceedings of 3rd International Beam Instrumentation Conference, IBIC14, Monterey, CA* (JACoW, Geneva, Switzerland, 2014), MOCYB03, pp. 12–15.

[10] Y. Liu, C. Long, and A. Aleksandrov, Real-time longitudinal profile measurement of operational H^- beam at the SNS linac using laser comb, in *Proceedings of the 10th International Beam Instrumentation Conference, IBIC2021, Pohang, Republic of Korea* (JACoW, Geneva, Switzerland, 2021), WEOA03, pp. 328–331.

[11] Y. Zhang, J. Galambos, and A. Shishlo, Measurement of longitudinal acceptance and emittance of the Oak Ridge Spallation Neutron Source Superconducting Linac, Phys. Rev. ST Accel. Beams **11**, 104001 (2008).

[12] A. Shishlo and A. Aleksandrov, Noninterceptive method to measure longitudinal Twiss parameters of a beam in a hadron linear accelerator using beam position monitors, Phys. Rev. ST Accel. Beams **16**, 062801 (2013).

[13] V. W. Yuan, R. C. Connolly, R. C. Garcia, K. F. Johnson, K. Saadatmand, O. R. Sander, D. P. Sandoval, and M. A. Shinas, Measurement of longitudinal phase space in an accelerated H^- beam using a laser-induced neutralization method, Nucl. Instrum. Methods Phys. Res., Sect. A **329**, 381 (1993).

[14] V. Scarpine, R. Campos, N. Eddy, B. Fellenz, T. Hamerla, J. Ruan, and R. Thurman-Keup, Beam profile measurements utilizing an amplitude modulated pulsed fiber laser at PIP2IT, in *Proceedings of IBIC2021, Pohang, Republic of Korea* (JACoW, Geneva, Switzerland, 2021), TUPP25, pp. 268–271.

[15] Y. Liu, A. Aleksandrov, S. Assadi, W. Blokland, C. Deibele, W. Grice, C. Long, T. Pelaia, and A. Webster, Nucl. Instrum. Methods Phys. Res., Sect. A **612**, 241 (2010).

[16] Y. Liu, C. Long, and A. Aleksandrov, Nonintrusive measurement of time-resolved emittances of 1-GeV operational hydrogen ion beam using a laser comb, Phys. Rev. Accel. Beams **23**, 102806 (2020).

[17] A. Shishlo and A. Aleksandrov, Longitudinal diagnostics methods and limits for hadron linacs, in *Proceedings of 5th International Beam Instrumentation Conference, IBIC2016, Barcelona, Spain* (JACoW, Geneva, Switzerland, 2016), WEAL01, pp. 563–567.

[18] http://energy.gov/downloads/doe-public-access-plan.